EXPERIMENTAL STUDY OF INTERFERENCE OF ROTOR MODELS AND TILT ROTOR AIRFRAME IN HOVER

N.N.Tarasov, head of department, TsAGI, Zukovsky, Russia

Abstract

Serious disadvantage of tilt rotor vehicle is that the rotor thrust in hover should be much greater than take-off weight. Additional rotor thrust is required to overcome the drag of wing being in the rotor air flow. Thrust losses may amount to 18-20% of rotor thrust making impossible the effective use of such vehicles.

The results of tests carried-out in TsAGI T-105 wind tunnel will be presented in the report. The objective of these tests was to study physical pattern of rotors and tilt rotors airframe interference as well as to search the means for decreasing the drag of wing in tilt rotor air flow in hover.

Basic physical studies were performed using wing model and tilt rotor models. Time-averaged induced velocities were measured in tilt rotor model downwash, which made it possible to get a rough notion of wing flow parameters On wing model were determined both total aerodynamic loads measured with the help of strain-gauge balance and distributed loads obtained by measuring static pressure on the wing surface. Diagrams of pressure distribution along the wing section in rotor downwash were correlated with diagrams in wind tunnel flow in the absence of rotors. Calculations of wing normal force in the rotor air flow were made using the measuring results of velocities in rotor downwash and wing surface pressure. Strip hypothesis was assumed in these calculations. Calculation results were compared with experimental results for the wing blown over by one or two rotors which made it possible to establish the main regularities of tilt rotor and wing interference. Investigations were performed for the two variants of rotating direction of tilt rotor models.

At the second stage the vehicle model with tilt rotors having a body and a wing with high-lift devices was tested. Model configuration allowed different types of high-lift devices to be investigated. The model was tested in the presence of single- and double-slotted flaps. Besides, special high-lift devices used in hover only were tested at wing leading edge. Relationships between thrust losses and single- and double-slotted flap angles were obtained. Optimum leading edge high-lift device angles were determined. These investigations were also performed for the two variants of rotating direction of tilt rotors. The range of low relative flight velocities was determined when high-lift devices at wing leading edge were not deflected. It was shown that the wing and airframe have no marked effect on tilt rotor aerodynamic characteristics.Experimental results revealed the main features of interference of rotor models and tilt rotor airframes in hovering. It was shown that the use of high-lift devices considerably decreased airframe blowing losses of rotor thrust in hovering and at vertical take-off. The use of high-lift devices for the tested tilt rotor vehicle configuration decreases rotor thrust losses from 20% to ~5% of thrust in hover which drastically changes vehicle characteristics at vertical take-off and essentially increases the payload.

1 Nomeclature

R – rotor radius

c – blade chord

k – the number of rotor blades

$\sigma = kc/\pi R$ – solidity coefficient

z_R – distance between rotor axes of rotation

l_w - wing span

b – wing chord

α_w – wing angle of attack

ω - angle rotary speed

W – rotor downwash speed

v_y – axial component of velocity

v_r – radial component of velocity

u – tangential component of velocity

α, β - downwash angles

V – wind tunnel flow velocity

ρ - air density

T – rotor thrust

M_k –rotor torque

Y - (airframe) wing normal force

$c_t = 2T/\rho(\omega R)^2\pi R^2$ – thrust coefficient

$m_k = 2M_k/\rho(\omega R)^2\pi R^2$ –torque coefficient

Dashes above length and velocity symbols mean that these values are divided by R or ωR respectively (for example $\bar{y}=y/R$ and $\bar{V}=V/wR$).

2 Inroduction

When designing the vehicle with tilt rotors it is important not only correctly to define drag of a wing and a body blown by a stream from rotors in hover but also to try to find ways of its reduction. The value of this drag depends on a configuration of blown surfaces, a relative positioning of these surfaces and rotors, distribution of the induced speed in rotor downwash and other factors as well. Great attention was paid to investigation of tilt rotor/airframe interaction. Results of some of these investigations are presented in papers [1]-[6]. Tilt rotor/airframe interaction was investigated at TsAGI in two stages. At the first stage the schematized model consisting of a rectangular wing without high-lift devices and tilt rotors the geometrical parameters of which were chosen on the basis of preliminary computations has been used. The purpose of this stage was to determine the main physical features of a flow about a wing by a stream from rotors in hover. At the second stage the hypothetical vehicle model with the tilt rotors having a fuselage, a wing with high-lift devices, a tail unit and the tilt rotor models has been investigated.

3 Test technique and equipment

Tests were performed in TsAGI T-105 wind tunnel. Rotor models were mounted at the universal rotorcraft test rig. Two sets of rotors were tested which differed only in solidity. The main geometrical characteristics of rotor models and their blades are as follows:

Rotor diameter D [m]	1.2
The number of blades of one rotor k	4
Blade section aerofoil	NACA 64-0XX
Rotor solidity coefficient 1σ_1…	0.089
Rotor solidity coefficient 2σ_2…	0.137

Rotor blades had a rectangular plan form, radius-variable thickness ratio t/c and geometric twist (Fig.1). Rotor hubs with remote collective-pitch control had alpha, delta and pitch-change hinges.

Thrust T and torque M_k acting on rotor models were measured using strain-gauge balance.

Time-averaged induced velocity and downwash angles were measured in isolated 1 rotor downwash using six-point pitot-static tube. Time-averaged induced velocity in rotor model downwash was measured at different distances from rotor plane of rotation:

$\bar{y}$= -0.08; -0.14; -0.18; 0.36.

When testing rotors in the presence of wing the rotors were mounted at the rig and the wing was fixed at the one-strut holder. The scheme of their relative position is shown in Fig.2. The main geometrical dimensions of the wing model of rectangular plan form are as follows:

Wing span l_w [m]	1.652
Wing chord b [m]	0.204
Wing airfoil section	Clark YH-20%

Wing normal force Y was measured using strain-gauge balance. Measurements of static pressure at lower and upper wing surfaces were performed in nine wing span sections.

The results of wing model tests at angles of attack α_w =-60°, -90°, -120° are presented as functions $\Delta \bar{P}=f(\bar{x})$, where $\bar{x}=x/b$ is a distance from airfoil nose to the current point on airfoil-section chord referred to the wing chord. The value of $\Delta \bar{P}$ was determined by the formula

$$\Delta\bar{P} = \frac{(P_l - P_0) - (P_u - P_0)}{0.5\rho V^2}$$

where P_l – the pressure at the lower wing surface, P_u – the pressure at the upper wing surface, P_0 – the static pressure. Test results for the wing model in the presence of rotors in hover are presented as functions $(P-P_0)=f(\bar{x})$ or $\Delta P=f(\bar{x})$ where $\Delta P=(P_l - P_0)-(P_u - P_0)$.

Airframe model layout and its main geometrical dimensions are shown in Fig.3. Airframe model had two variants of wing high-lift devices. The first variant (Fig.4) included a deflected nose, a flap and a single-slotted flap. The second variant (Fig.4) included a deflected nose and a double-slotted flap. Photography of the model is shown on fig. 5.

In hover mode the normal force **Y** was measured on airframe model using built-in strain-gauge balance.

To investigate the flow pattern over airfoil with deflected nose, a flap and a single-slotted flap the wing section model with chord b=0.14 m, wing span l_w = 0.22 m and airfoil NACA 63-218 was made. Airfoil flow patterns with deflected and undeflected (open and closed) high-lift devices at the angle of attack α_w=-90° were obtained in smoke wind tunnel.

4 Test results

Polars for an isolated rotor as well as polars obtained during the combined operation with another rotor are presented in Fig.6. It is seen that due to comparatively large distance between rotor axes ($\bar{z}_R$=2.5) the rotors do not influence each other. The presence of the wing model has no any noticeable effect on rotor aerodynamic characteristics either. The same result was obtained when rotors were tested in the presence of airframe model (Fig.7). This is evidently explained by tilt rotor blade aerodynamic configuration features (high blade twist and rather large value of rotor disk-averaged lift coefficient in hover) as the wing has a pronounced effect on helicopter rotor aerodynamic characteristics.

Thus, isolated rotor aerodynamic characteristics can be used when calculating the hover mode and vertical take-off of aircraft with tilt rotors of the considered type.

In Fig. 8 components of induced velocity in tilt rotor downwash are presented for one of the rotor operating modes. It is seen that in contrast to axial induced velocity distribution in helicopter rotor downwash the tilt rotor axial velocity in tilt-rotor downwash is distributed more uniformly over the stream radius.

Using the measurement results of induced velocity in isolated rotor downwash in hover the velocity field of "undisturbed" (by the wing) flow is determined in the downwash area where the wing is during rotor and wing combined operation. Wing span distribution of chord-averaged velocity values $v_{xy\ av}$ and chord-averaged inflow angles α'_{av} is presented in Fig.9.

It is natural that the wing immersed in rotor downwash will change the velocity field obtained from velocity measurements in isolated rotor downwash. However if we assume that wing disturbances in rotor downwash are approximately the same as isolated wing disturbances at corresponding angles of attack then we may use the measurement results of induced velocities in isolated rotor downwash and aerodynamic characteristics of isolated wing sections at corresponding angles of attack to calculate the force acting on the wing. It is evident that the angle of attack of the wing section immersed in rotor downwash depends on direction of rotation and is defined by the inflow angle. When direction of rotation corresponds to the external blade advance (the blade approaches the wing from the leading-edge) the wing section angle of attack α_w =-90°+ α'_{av}. When direction of rotation corresponds to the internal blade advance (the blade approaches the wing from the trailing edge) the wing section angle of attack α_w =-90°-α'_{av}.

In accordance with values of chord-averaged inflow angle shown in the diagram in Fig. 9 the wing section angles of attack vary over the range from -105° to -120° at direction of rotation with internal advance, and from -60° to -75° at reverse direction. Aerodynamic characteristics of isolated wing sections over the range of angles of attack from -60° to -120 °

were obtained from measurements of static pressure on the wing surface. The static pressure measurement results are presented in diagrams (Figs. 10-12). It should be noted that at α_w =-90° and -120° the pressure distribution on airfoil nose section is such that component of force acting on this part of airfoil is positive.

In these figures also presented diagrams of wing span load distributions $\Delta\ \bar{Y}$ The value of $\Delta\ \bar{Y}$ was defined by integration:

$$\Delta\bar{Y} = \int \Delta\bar{P}\,d\bar{x}$$

The load dramatically decreases near the wing tips and has a smooth minimum in the central part of the wing. The results of determining the component values ΔY show that load decrease in the central part of the wing is induced by the pressure increase on the lower surface.

Measurement results of normal force Y acting on the wing model blown over by one or two rotors are presents in Fig 13. It is seen that the value of relative normal force $\bar{Y}$=Y/T and $\bar{Y}$=Y/2T, where 2T is the sum of two rotors thrust, does not depend on rotor thrust coefficient. Furthermore the $\bar{Y}$ of the wing blown over by one rotor is not equal to the $\bar{Y}$ of the wing blown over by two rotors.

To find out the reasons of this phenomenon it is necessary to know about the load distribution along the wing surface. Diagrams of static pressure distribution in different wing span sections blown over by one or two rotors for the two variants of rotating direction are presented in Fig 14, 15.

For the sake of ease of analysis the diagrams can be conventionally divided into three groups. To the first group refer the diagrams of static pressure distribution in sections I and II located under rotor root and under its hub (see Fig.3). In these sections mainly the rear part of airfoil is loaded.

To the second group refer the diagrams of static pressure distribution in sections III, IV, V which have the same pattern of pressure distribution as in isolated wing sections at high negative angles of attack.

To the third group refer the diagrams obtained in sections VI–IX. Despite the different patterns of pressure distribution in each of these sections the general regularity can be singled out: in all these sections there is a suction peak in the nose or rear part of airfoil depending on direction of rotation.

The analysis showed that in the area of sections I and II ($\bar{z}$=1.15 and 1.05) the distribution of velocity v_{xy} is such that the rear part of airfoil chord should be blown over with the greatest speed. Correspondingly in diagrams referred to the first group a higher pressure is observed in the rear part of the chord.

In the range of 0.55< $\bar{z}$<0.95 i.e. in the area of sections III, IV, V the chord velocity v_{xy} is constant and the pattern of static pressure distribution in sections referred to the second group is approximately the same as of isolated wing.

Thereby it is of interest to compare diagrams ΔP=f(x) obtained for the wing in flow and for the wing blown over by rotor in hover. As an example of such comparison the diagrams are presented in Fig.16 showing that diagrams ΔP=f(x) of isolated wing differ but little from the diagrams obtained at the wing in the presence of rotor.

Quite different pattern is observed in sections VI–IX. Section VI location corresponds to the external boundary of isolated rotor downwash other sections are located outside this boundary. The load in these sections is not equal to zero therefore part of air thrown off by rotors is spreading along the wing span. When testing the wing in the presence of one rotor at a distance from the section located at the jet boundary that was defined for isolated rotor, the load decreases in central sections of the wing (section VII–IX).

When testing the wing in the presence of two rotors the interaction of flows spreading along the wing span results in a considerable increase of load in the central part of the wing and a relatively small increase of load in other sections.

The value of load in different wing span sections was determined by integrating the pressure values on the wing surface with respect to chord. Wing span load distribution Δ**Y** is shown in Fig. 17. The general increase of the wing drag due to interaction of air flows thrown off by two rotors makes up 20% when direction of rotation corresponds to the external blade advance and 16 % at direction of rotation with internal blade advance.

Let us compare the wing span load distribution obtained when testing the wing in the presence of one rotor to the load distribution obtained by computation using measurement results of induced velocity in isolated rotor downwash and measurement results of static pressure on the surface of isolated wing. The computation was performed for the rotor and wing relative position shown in Fig.3. Wing-span load for the wing in the rotor downwash was determined by a formula

$$\Delta Y_1 = \Delta \bar{Y}_1 \frac{\rho(\bar{v}_{xy})^2}{2} \cdot b(\omega R)^2$$

Velocity v_{xyav} for each wing section was taken from diagram in Fig.9, and the value of ΔY coefficient from diagrams in Figs. 10 – 12 in view of direction of rotation. Velocity of blade tips was assumed the same as in tests of rotor in the presence of wing. Calculation results for the direction of rotation with the external blade advance are presented in Fig. 18. Wing normal force obtained during calculation is approximately 1.4 times less than the normal force measured on the wing model with strain-gauge balance and that obtained by the results of static pressure measurement. The difference between calculation and test results is basically due to a greater load in wing sections near the external stream boundary of isolated rotor. Load increase as compared to calculation is caused by the fact that part of airflow blown off by rotor is spreading along the wing span; this phenomenon was not taken into account during computation.

Thus, measurement results of induced velocity in isolated rotor downwash and of static pressure on the surface of the wing model blown over by rotor made it possible to find out the main features of rotor/wing interaction for vertical takeoff aircraft in hover.

Quantitative data of tilt rotors effect on aerodynamic characteristics of airframe in hover were obtained while testing rotor models and airframe with two types of high-lift devices. In the course of tests it was obtained that airframe relative normal force $\bar{Y}$ practically does not depend on rotor thrust coefficient (Figs. 19) for both types of high-lift devices. Positions of wing high-lift device components were defined at which airframe normal force had minimum absolute values for the two variants of rotating direction.

As an example in Fig. 20 are presented diagrams of airframe relative normal force variation at different angles of one-slotted flap and the links of double-slotted flap. Deflection of one-slotted flap by 90° increases airframe relative normal force from -0.18 to -0.11, and deflection of double-slotted flap main link by 85° increases Y approximately to -0.125. It is known that airframe relative normal force in hover depends on the value of relative blown over area. It should be noted that the value of relative blown over area of the tested airframe model for undeflected high-lift devices was $S_{bl} = b_w R/\pi R^2 \approx 0.15$, with one-slotted flap deflected by 90° $\mathbf{S_{bl}} \approx 0.11$ and with double-slotted flap deflected by 85° $S_{bl} \approx 0.12$.

Values of airframe relative normal force at optimum deflection angles of wing high-lift device components as well as optimum angles of wing high-lift device components deflection are presented in Figs. 21. It is seen that using high-lift devices with one-slotted flap the flap makes it possible to increase the airframe normal force approximately to -0.09, and the deflected nose – to -0.05 ÷ -0.06 depending on the direction of rotation. When high-lift devices with a double-slotted flap are used a deflector deviated by 35°does not change the airframe relative normal force measured under deflection of the main link by 85°, and the deflected nose decreases the force Y down to -0.08 ÷ -0.10 depending on direction of rotation.

It is interesting to note that smaller absolute values of airframe relative normal force with deflected high-lift devices in hover were obtained at rotating direction corresponding to the internal blade advance.

Comparing test results obtained for airframe model with two types of high-lift devices we see that in hover one-slotted flap, panel and deflected nose appear to be more effective for increasing airframe normal force than the deflected nose and double-slotted flap.

It was also obtained that with undeflected high-lift devises the absolute value of normal force of airframe blown over by one rotor is three times less than the absolute value of normal force of airframe blown over by two rotors. With deflected high-lift devices the normal force of airframe blown over by one rotor is approximately two times as less than the normal force of airframe blown over by two rotors.

Relative normal forces with undeflected high-lift devices differ by 50% and with deflected high-lift devices – approximately by 10% respectively (Fig. 22).

Increase of absolute value of airframe normal force caused by the interaction of rotor flows spreading about the wing to a great extent depends on wing reference chord value at constant distance between rotor axes. When testing rotor models and the wing with reference chord of 0.35 the force Y decreased by 20%, and when testing airframe model with wing reference chord of 0.5 the force Y decreased by 50%.

Evidently with deflected high-lift devices the pattern of rotor flows spreading about the wing changes substantially and airframe normal force decreases but little.

Since wing airfoil configuration with deflected high-lift devices essentially differ from the conventional shape of aerofoil profile it was necessary to find out how the deflected nose and the lifted flap influence airframe aerodynamic characteristics in acceleration conditions at low flight speed. For this purpose airframe model was tested with rotors at geometric angle of attack α=0 and two positions of high-lift devices components:

- commonly used flap deflection for increasing the wing lift at take-off δ_f=30°;
- optimum position of high-lift devices components in hover δ_f =-90°; δ_f =-60°and δ_u=-30, δ_l =-60° in terms of decreasing airframe normal force absolute value.

Results of these tests are presented in Fig. 23. It is seen that at $\bar{V}$=0.08 the positive effect of flap and deflected nose disappears, so even at low horizontal flight velocity in acceleration conditions these high-lift device components should be closed.

To illustrate the pattern of flow over wing airfoil at angle of attack α_w =-90° with deflected and undeflected high-lift devices smoke spectra are shown in Fig.24. Airfoil wake width with deflected high-lift devices is approximately two times less than with undeflected high-lift devices. Therefore airfoil drag with deflected high-lift devices should be substantially smaller which was proved in the course of testing the airframe model with rotors in hover.

5 Conclusions

Test results made it possible to find out the main features of interaction of rotor models and airframe of vertical takeoff aircraft in hover.

The use of wing high-lift devices substantially decreases rotor thrust losses for airframe blowing in hover and vertical take-off modes. For the given configuration this decrease of losses makes 12-13% of isolated rotors total thrust (from 18% to 5-6%).

REFERENCES

1. McCroskey, W.J., Spalart, Ph., Laub, G.H., Maisel, M.D., and Maskew, B., “Airload on Bluff Bodies, with Application to the Rotor Induced Download on Tilt-Rotor Aircraft,” Ninth European Rotorcraft Forum, Stresa, Italy, September 13-15, 1983.
2. Felker, F.F. and Light, J.S., “Aerodynamic Interaction Between a Rotor and Wing in Hover, ”*Journal of the American Helicopter Society,* Vol.33, No.2, April 1988, pp. 53-61.
3. McVeigh, M.A., Grauer, W.K., and Paisley, D.J., “Rotor/Airframe Interaction on Tilt-Rotor Aircraft,” ”*Journal of the American Helicopter Society,* Vol.35, No.2, April 1990, pp. 43-51.
4. Felker, F.F., “Wing Download Results from a Test of a 0.658-ScaleV-22 Rotor and Wing,” ”*Journal of the American Helicopter Society,* Vol.37, No.4, October 1992, pp. 58-63.
5. Swanson, A.A. and Light, J.S., “Shadowgraph Flow Visualization of Isolated Tiltrotor and Rotor/Wing Wakes,” American Helicopter society 48th Annual Forum Proceedings, Washington, DC, June 3-5, 1992, pp. 1323-1344.
6. Wood, T.L. and Paryea, M.A., “Reduction of Tiltrotor Download” American Helicopter society 49th Annual Forum Proceedings, St. Louis, MO, May 19-21, 1993, pp. 1177-1191.

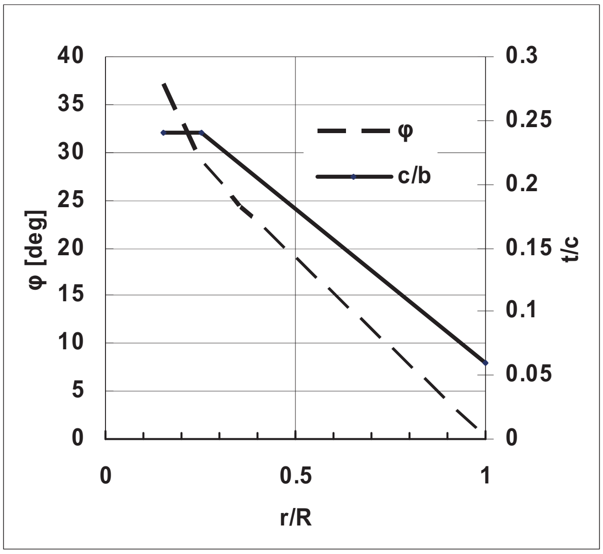

Figure 1. Geometric twist of the blade and thickness ratio **t/c**

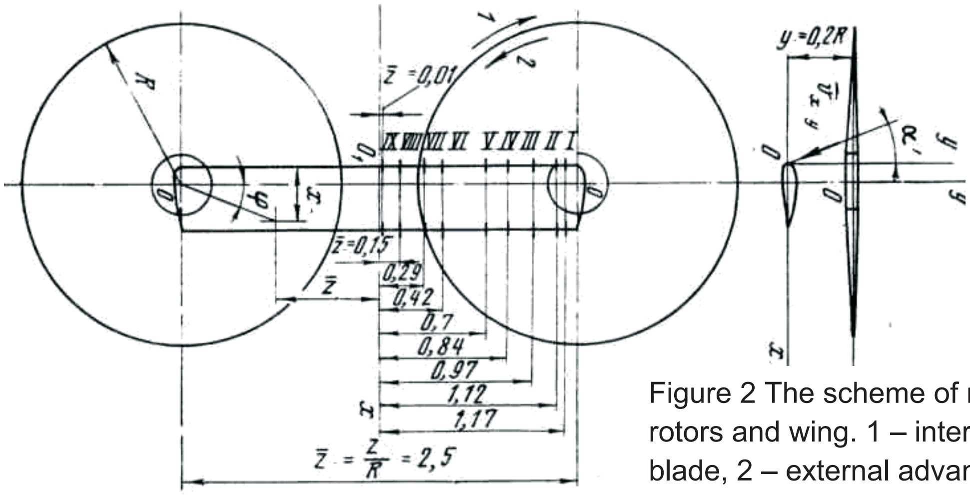

Figure 2 The scheme of relative position rotors and wing. 1 – internal advance of blade, 2 – external advance of blade

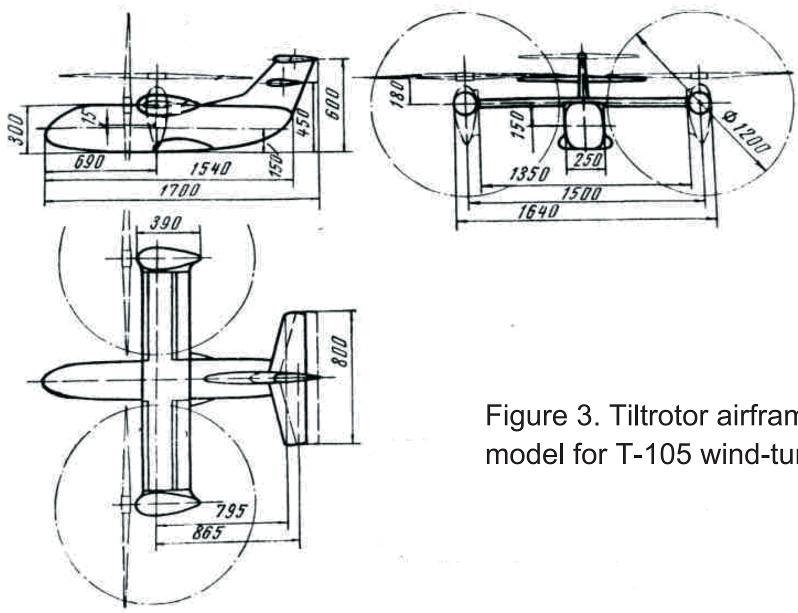

Figure 3. Tiltrotor airframe model for T-105 wind-tunnel.

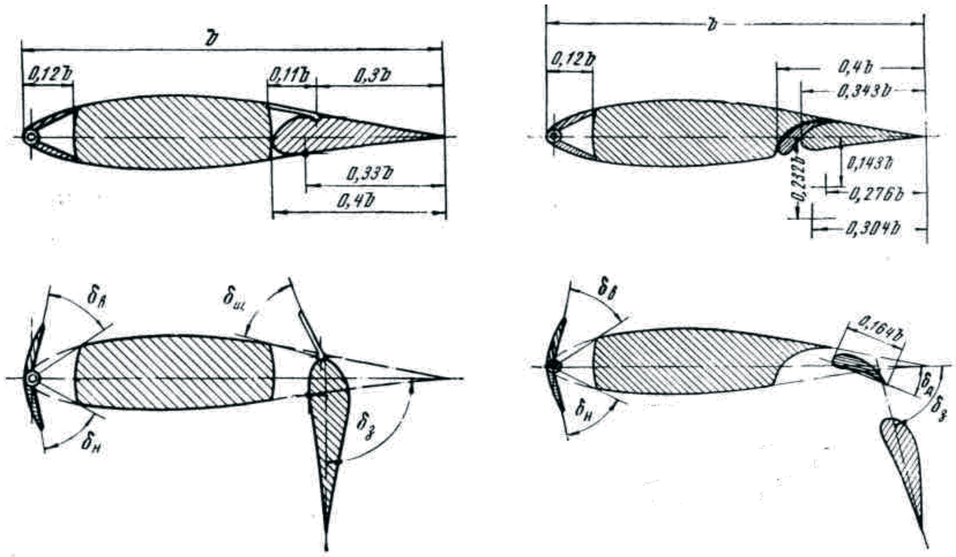

Figure 4. Two variants of high lift devices of the tiltrotor model.

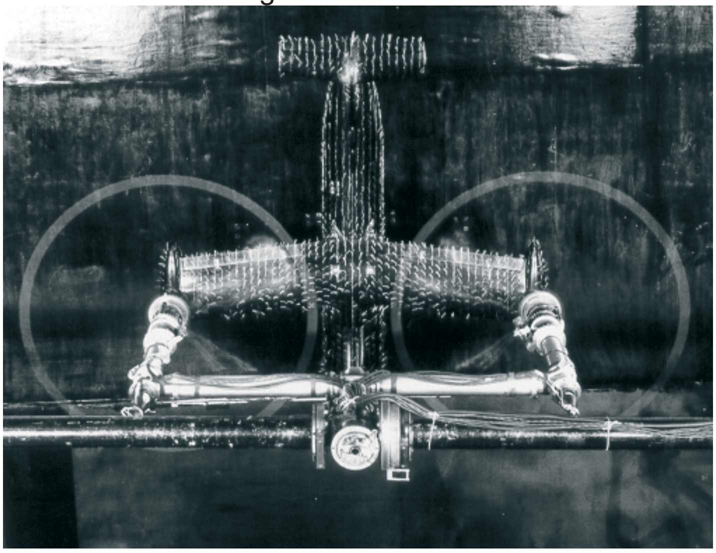

Figure 5 Tilt rotor model it T-105 wind tunnel

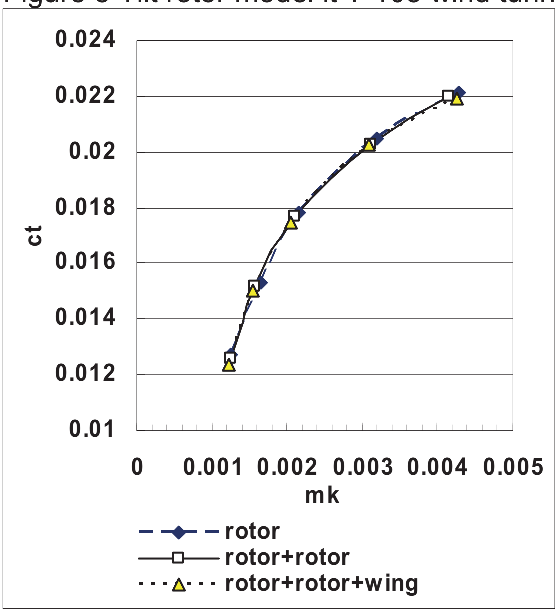

Figure 6. Polars of model rotors with wing.

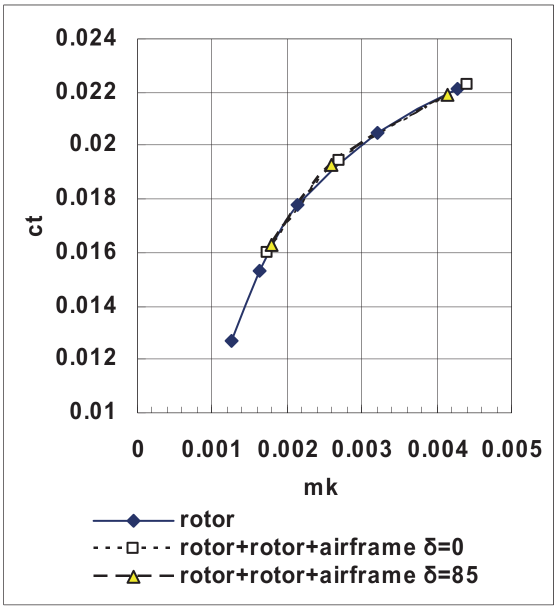

Figure 7. Polars of model rotors with airframe

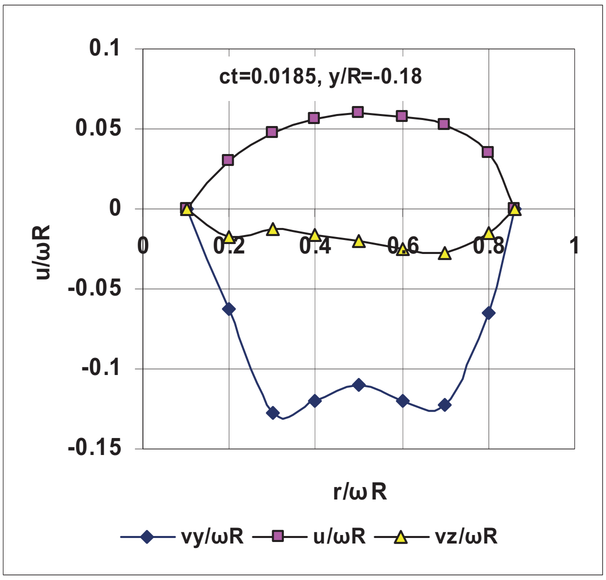

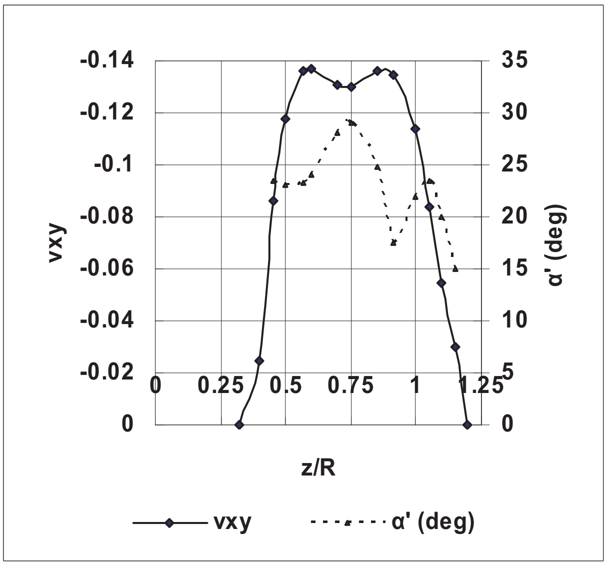

Figure 8. Components of induce velocity in tilt rotor downwash

Figure 9. Wing span distribution of chord-averaged velocity $\mathbf{v}_{xy\ av}$ and chord-averaged inflow angles α'_{av}

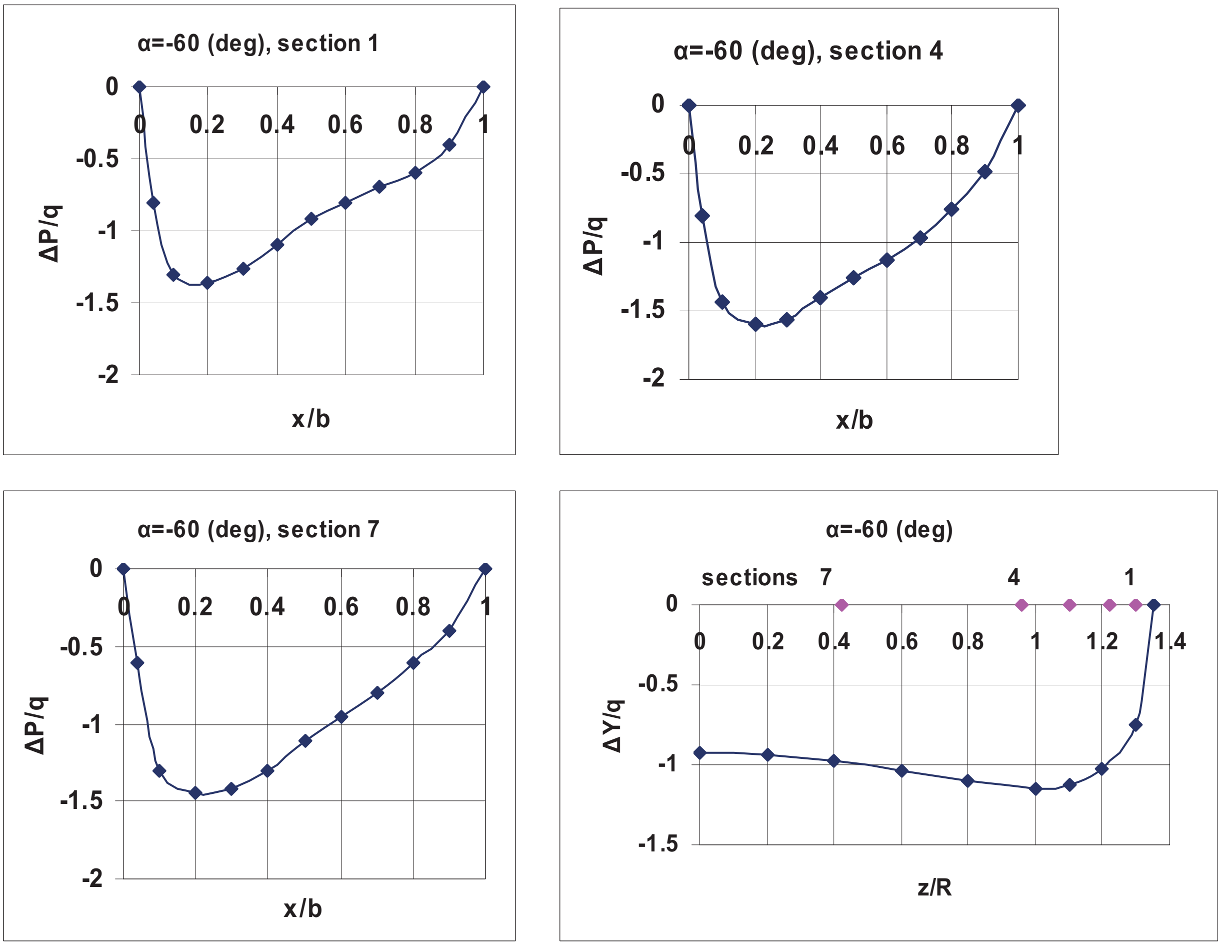

Figure 10. Load distribution on the chord and span of wing

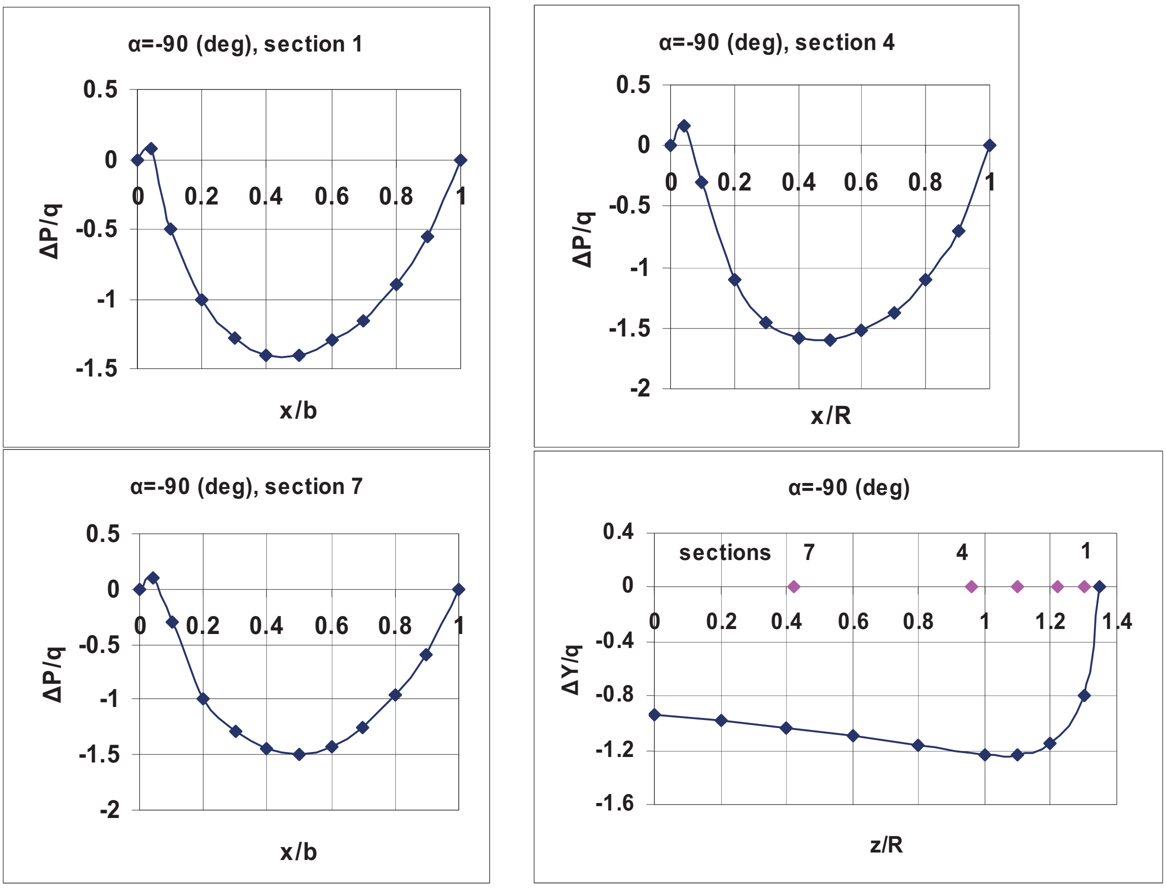

Figure 11. Load distribution on the chord and span of wing

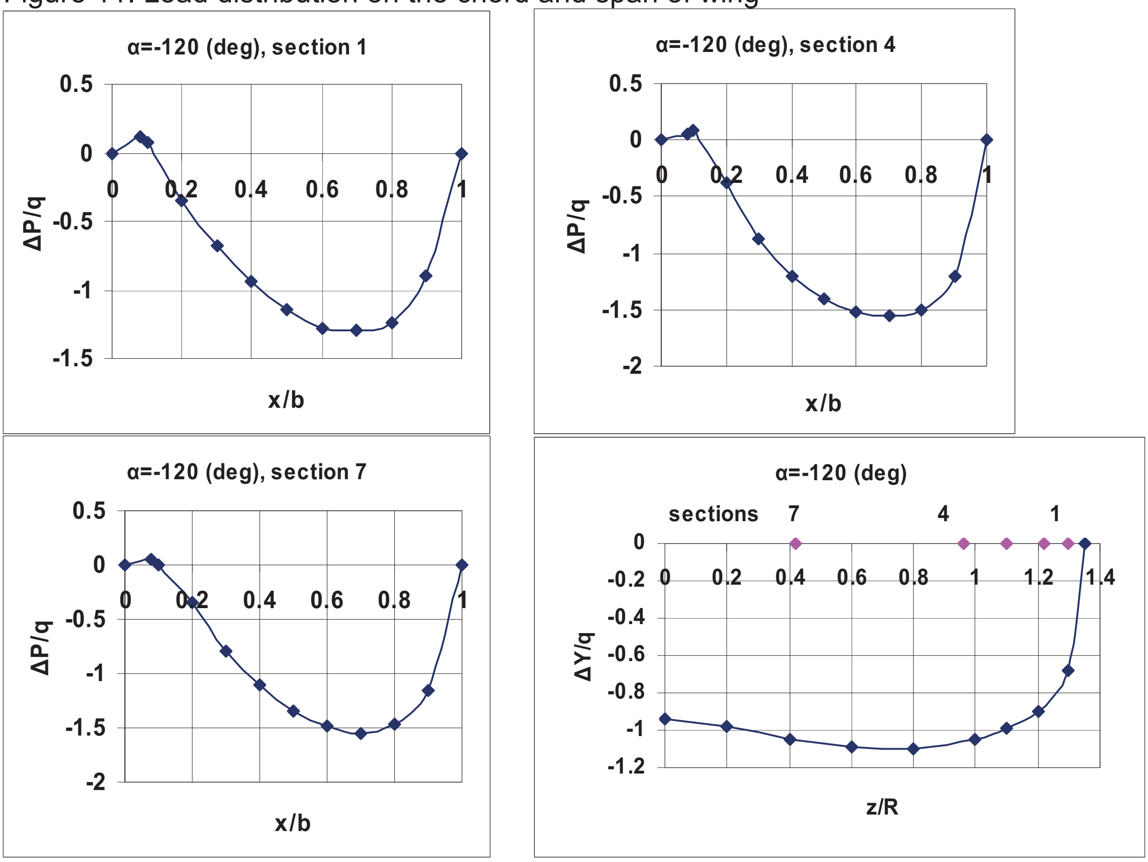

Figure 12. Load distribution on the chord and span of wing

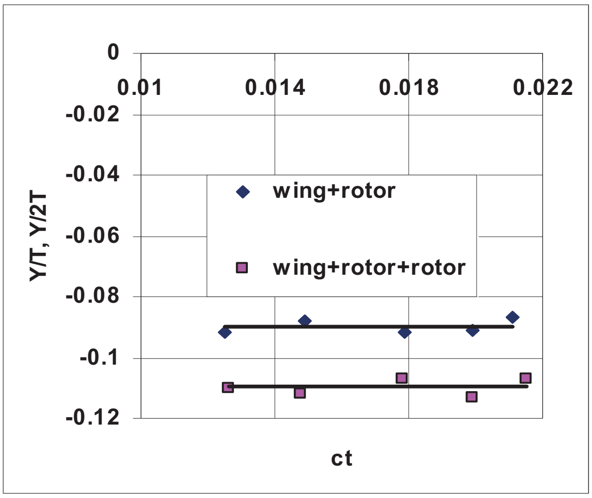

Figure 13. The normal force on the wing.

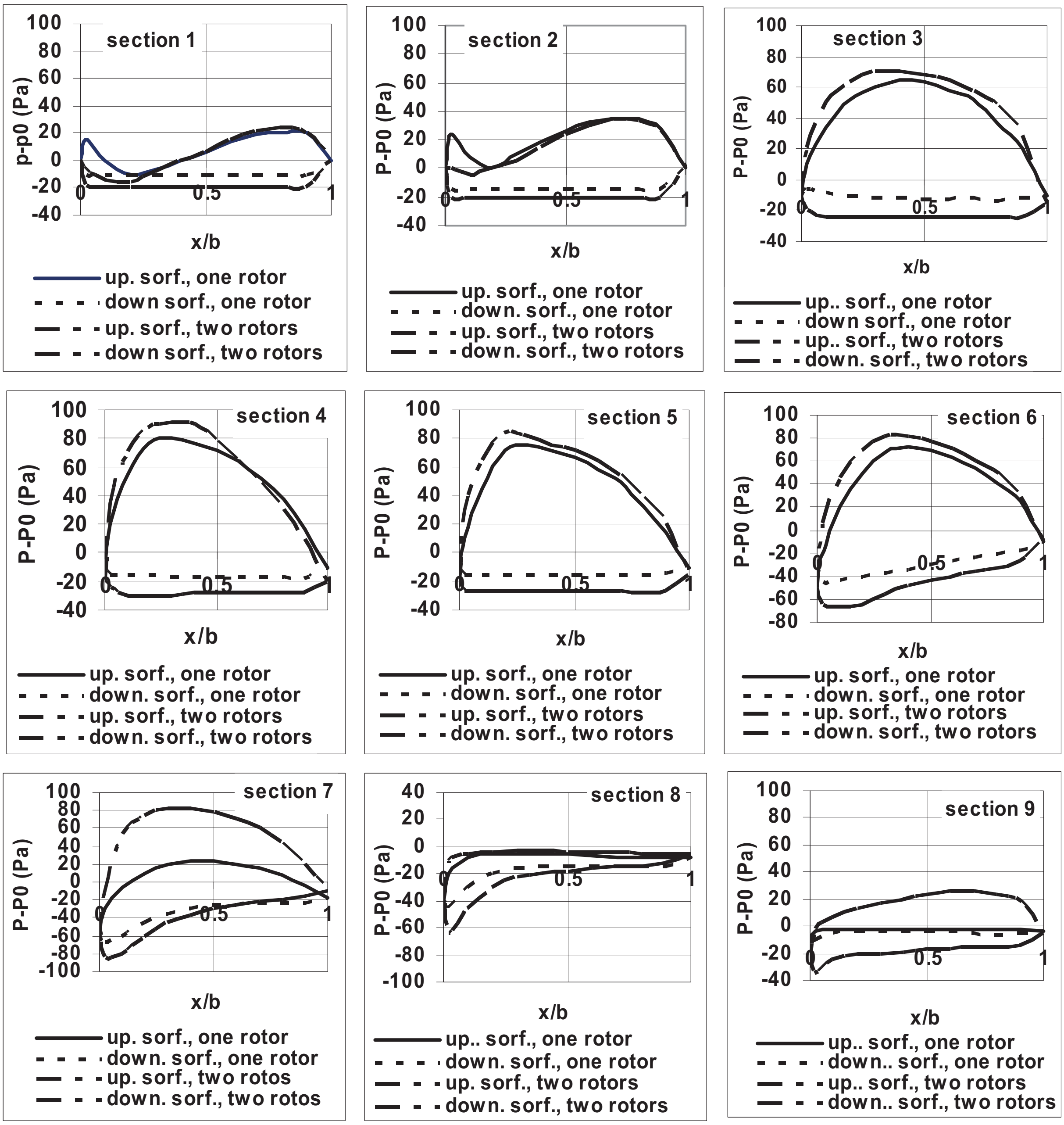

Figure 14. Load distribution on the chord of wing for external blade advance.

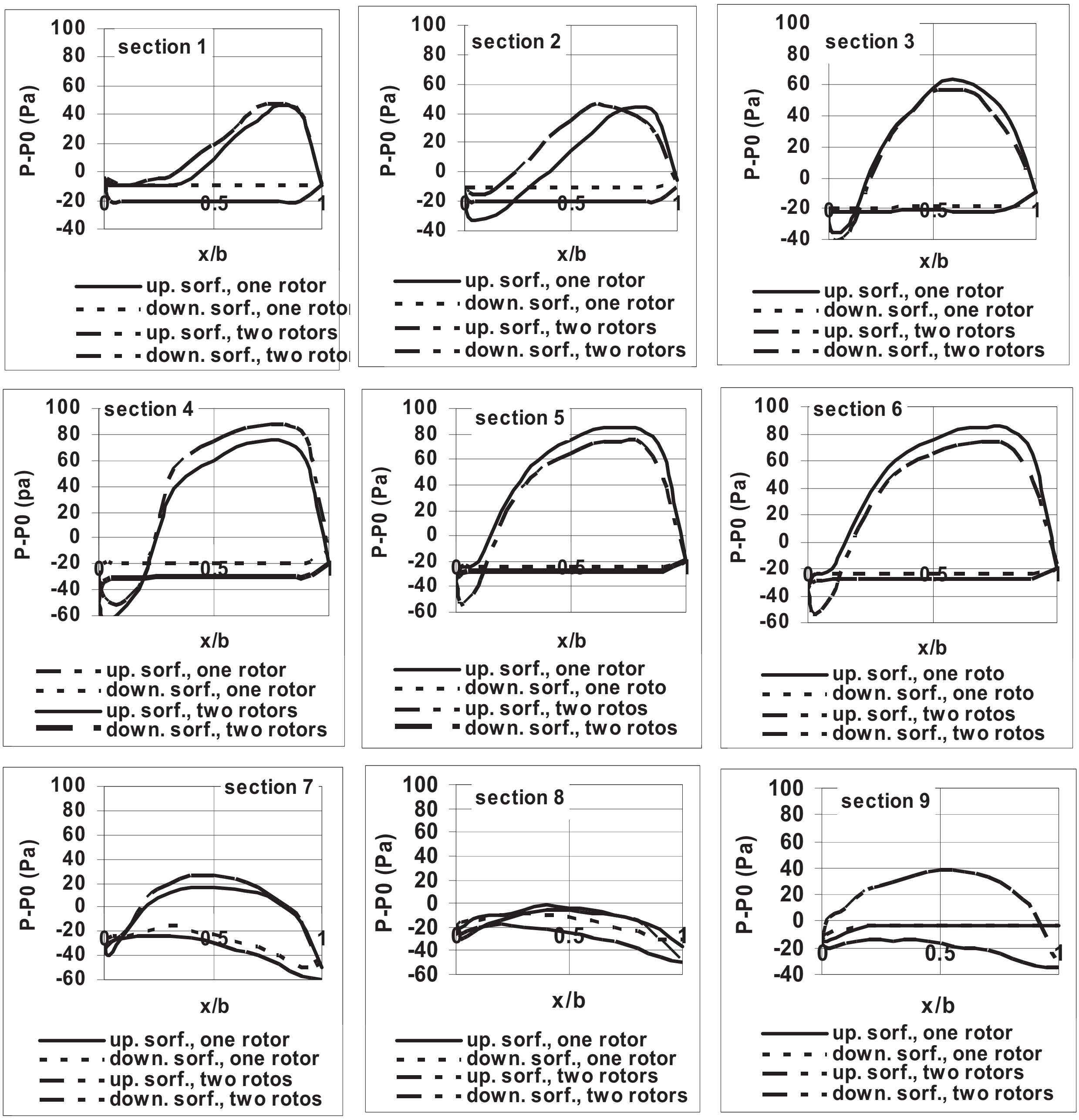

Figure 15. Load distribution on the chord of wing for internal blade advance.

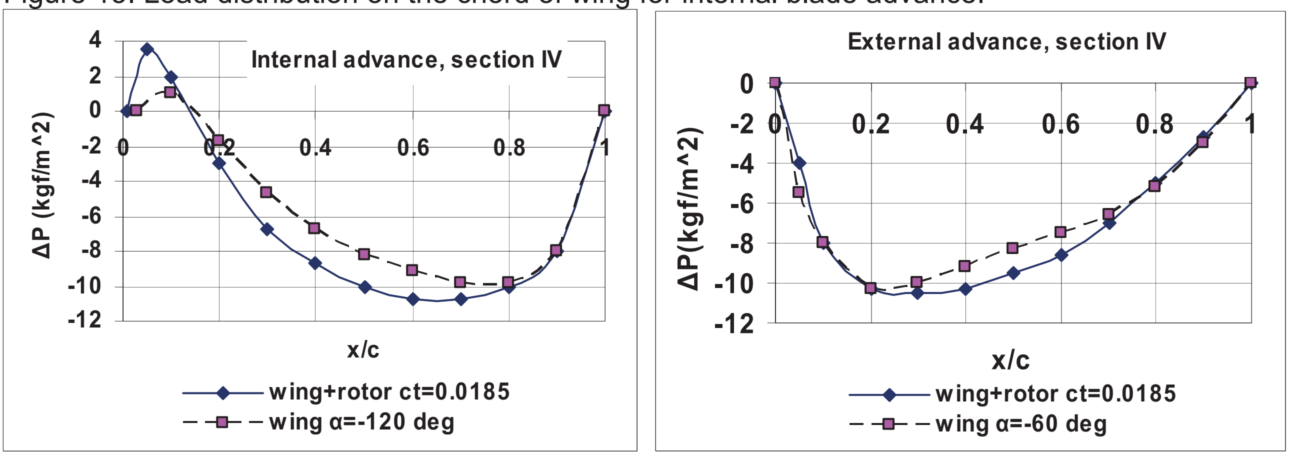

Figure 16. Load distribution on the chord of the wing and the wing blown over by the rotor.

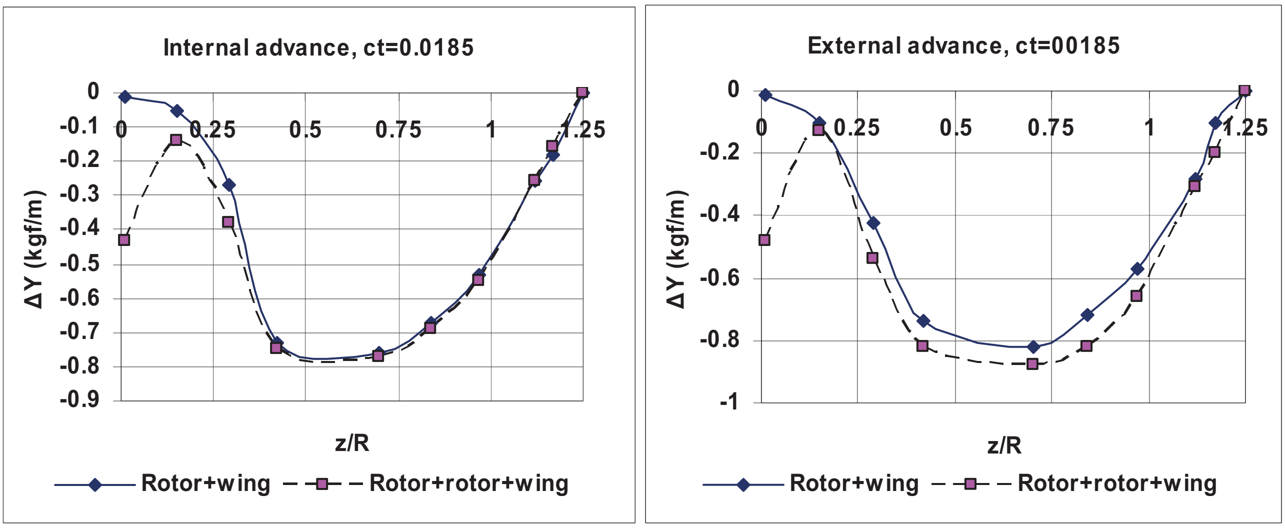

Figure 17. Load distribution on the span of the wing blown over by one or two rotors.

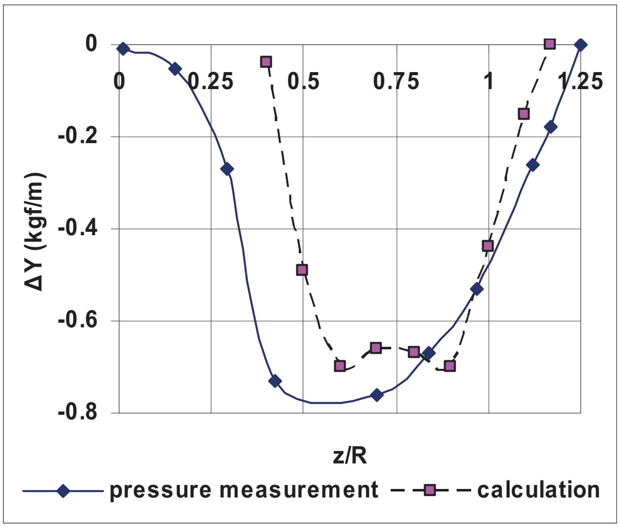

Figure 18. Calculation and measurement results of load distribution on the span of the wing blown over by one rotor.

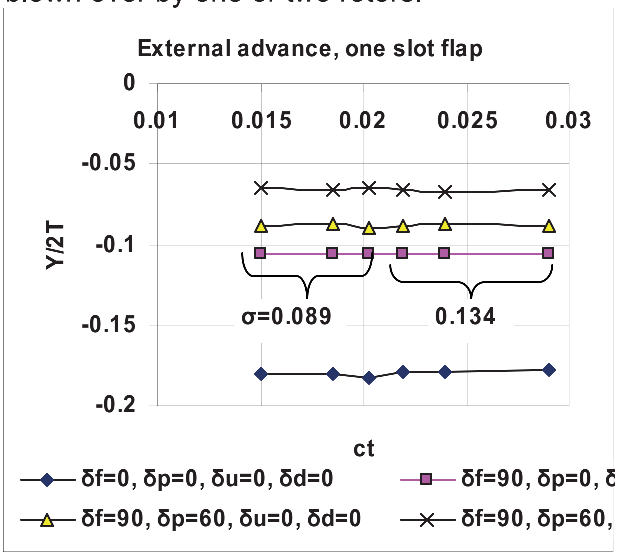

Figure 19. Influence the rotor thrust coefficient on airframe relative normal force.

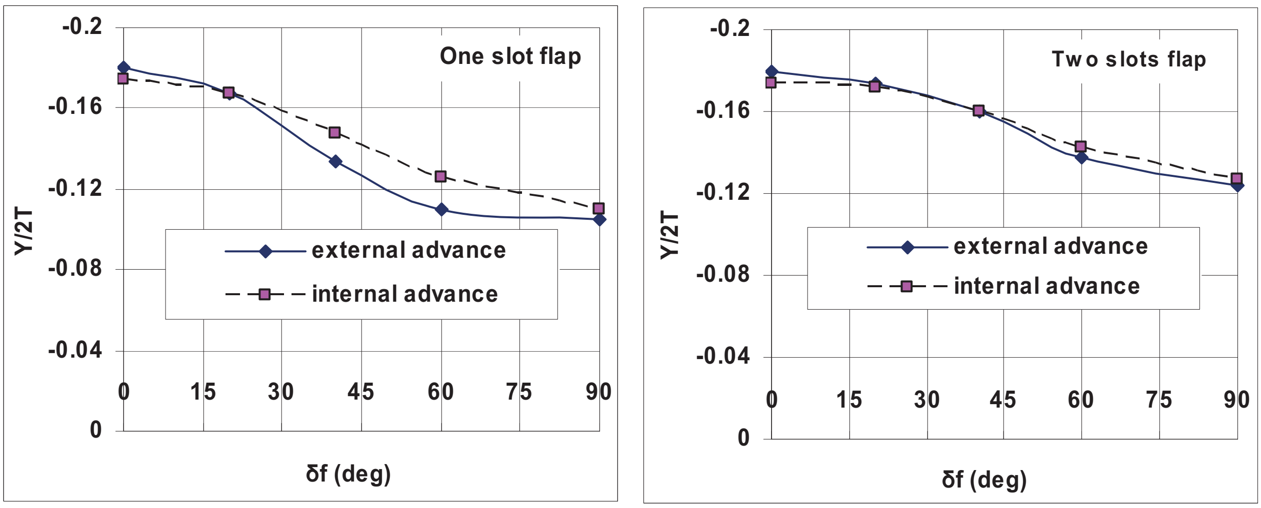

Figure 20. Airframe relative normal force variation at different angles of one-slotted flap and the links of double-slotted flap.

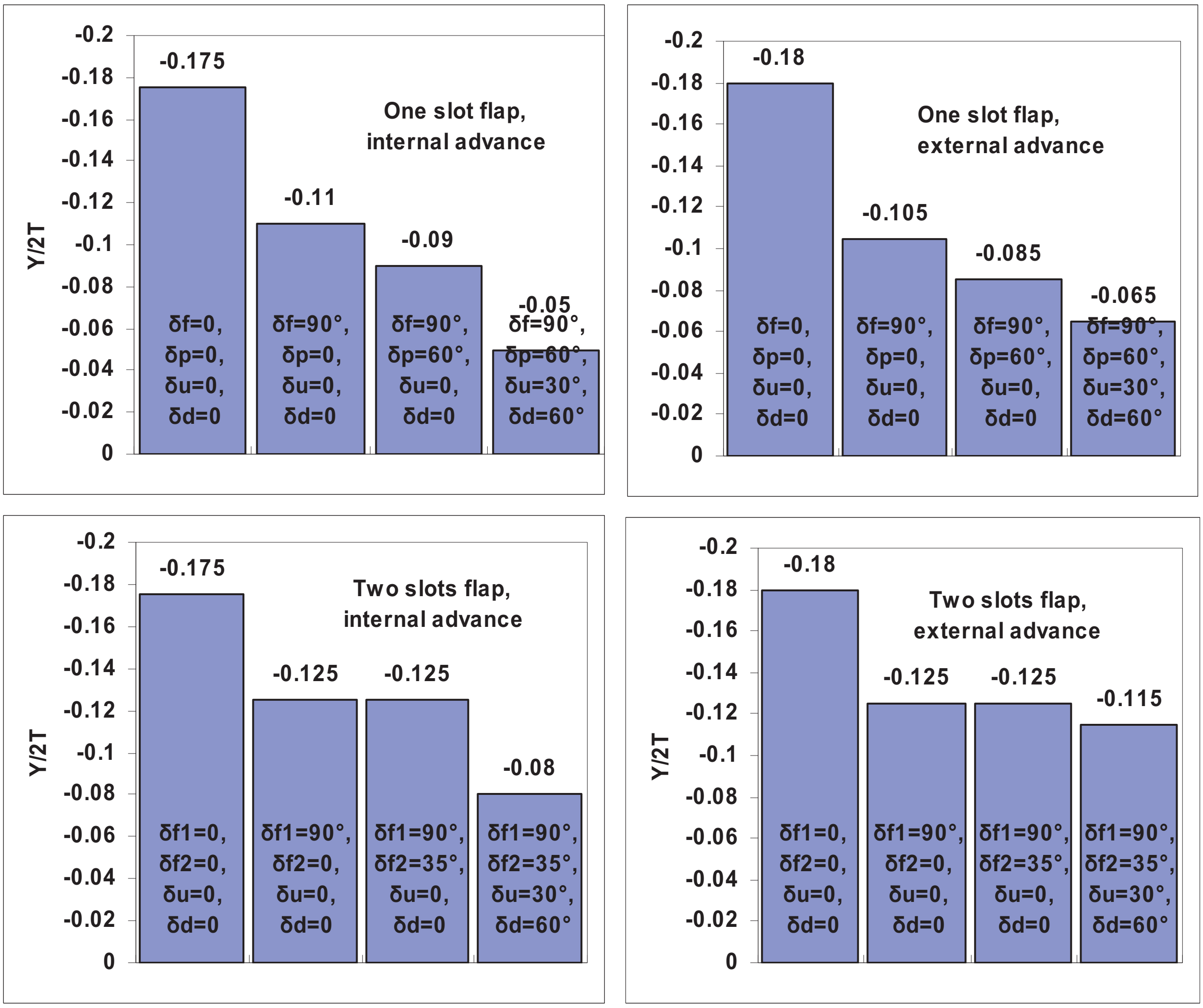

Figure 21. Values of airframe relative normal force at optimum deflection angles of wing high-lift device components.

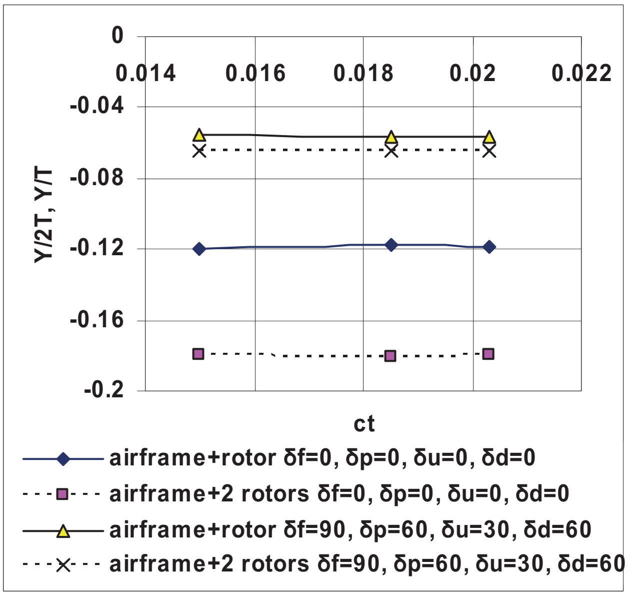

Figure 22. One and two rotors interaction with airframe

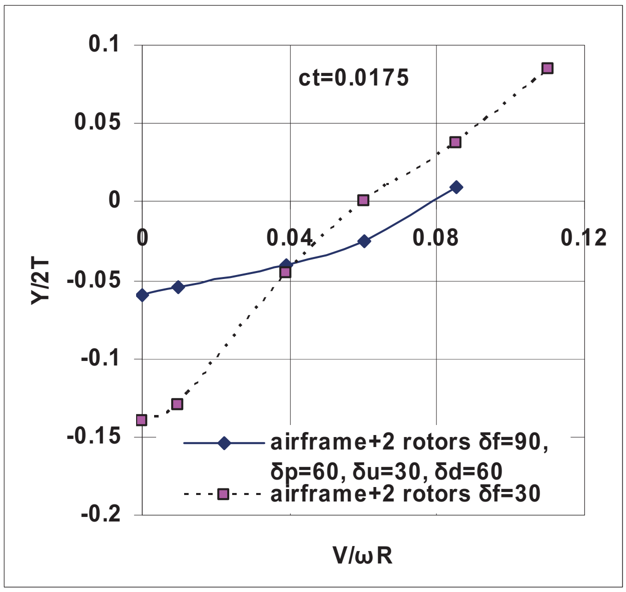

Figure 23. Influence of the relative velocity on the airframe normal force for different high-lift device deflection

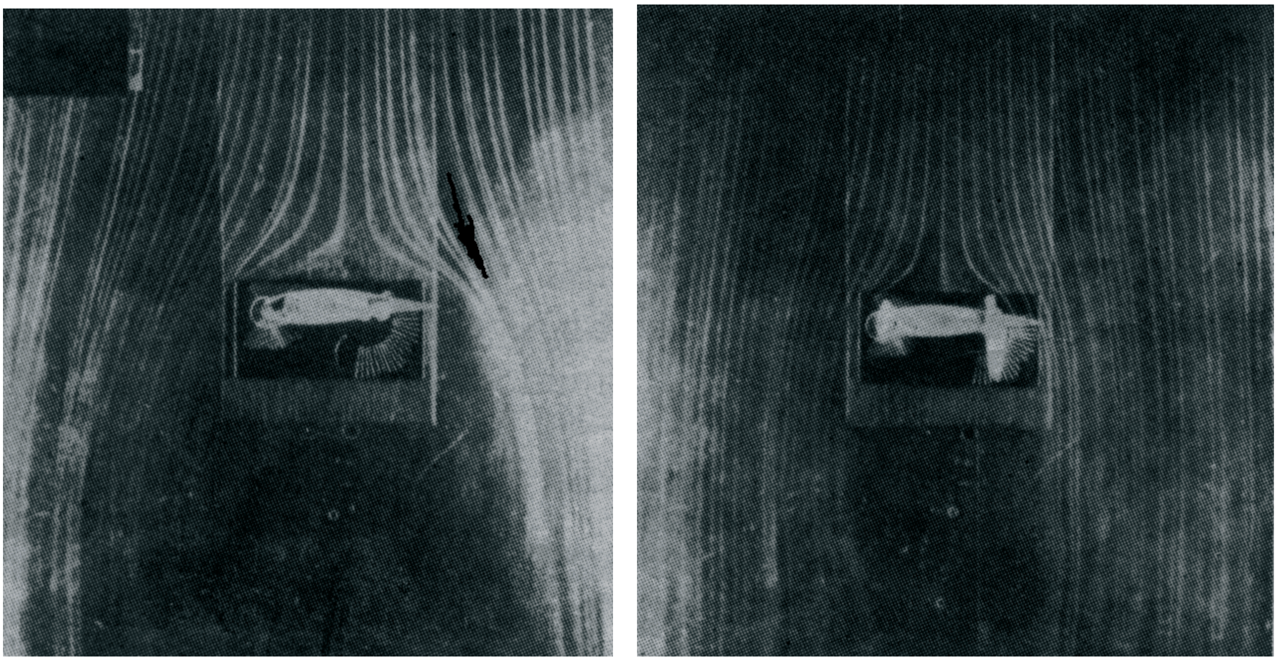

Figure 24. The smoke spectra of the airfoil with deflected and undeflected high-lift devices.